J Mater Sci (2009) 44:3633–3642
DOI 10.1007/s10853-009-3469-9

Characterization of phase transformations and shape memory behavior of Fe–27.79Mn–2.72Si (wt%) alloy by thermomechanical and thermal treatments

Murat Eskil · Mehmet Ceylan

Received: 22 February 2009 / Accepted: 6 April 2009 / Published online: 30 April 2009

Abstract Magnetic properties and volume fraction of the phases of a Fe–27.79Mn–2.72Si (wt%) alloy have been investigated by Mössbauer spectroscopy. The microstructure has been investigated using transmission electron microscope, scattering electron microscope, and light optical microscope. The stress-induced martensitic transformation, shape memory behavior, and shape recovery processes have been studied through the differential scanning calorimetry (DSC), tensile, and bending tests. The specimen was treated by the repetition of small amount of tensile deformations at room temperature, followed by a subsequent annealing at 600 °C at every cycle for bending and tensile tests. During the tensile tests, Vickers hardness values were determined for every step of thermomechanical treatments. At low deformation rate, the shape memory effect is almost complete Bergeon et al. (A242:87, 1998), so low deformation rate was studied in this work. Bending test was another thermomechanical training procedure to see the recovery rate for this investigation.

Introduction

Fe–Mn–Si alloys, as a possible alternative for the expensive Ti–Ni alloys, have received considerable attention in the past 20 years and possibly they may become a new class of shape memory alloys (SMAs) of great technical importance with a high potential for engineering applications [1, 2]. However, they have not got any important applications although they have low cost, good workability, good machinability, and good weldability [1]. Low cost Fe–Mn–Si based SMAs have the disadvantage of incomplete shape recovery. Much research has been done to improve their shape recovery, by means of a special thermomechanical treatment called ‘training’ [3] and by the addition of other elements [4, 5]. The training raises the production cost of Fe–Mn–Si based SMAs and severely limit their industrial applicability. By deforming the material, the fcc (γ) → hcp (ε) stress-induced martensitic transformation takes place. During subsequent heating, the reverse $\varepsilon \rightarrow \gamma$ transformation occurs. Not only the initial γ-fcc crystal is obtained but also the initial shape is partially recovered [3], so shape memory experiments consist of inducing the martensitic transformation from fcc to hcp by straining the material at room temperature and subsequently heating the samples up to a sufficiently high temperature in order to complete the reverse transformation [6]. Kajiwara et al. [7, 8] studied the microstructures of stress-induced martensite of specimens subjected to thermomechanical training in detail. They came to a conclusion that, in order to obtain a good shape memory effect, the austenite must contain high densities of stacking faults distributed uniformly on the primary slip system. Under the external stress the stress-induced martensite can nucleate easily at those pre-existed stacking faults and the thin martensite plates with good reversibility can be produced. Thus, a good SME can be expected [9].

In this work, DSC, tensile test, and bending tests will be used to measure and characterize shape memory behavior of a Fe–27.79Mn–2.72Si–0.12V (wt%) alloy and different microstructures taken from different cooling treatments

---

M. Eskil (✉)
Muallim Rifat Education Faculty, Kilis 7 Aralik University,
Kilis 79000, Turkey
e-mail: eskil_m2001@yahoo.com

M. Ceylan
Department of Physics, Faculty of Science and Arts,
Firat University, Elazig 23169, Turkey

were investigated by using transmission electron microscope (TEM), scattering electron microscope (SEM), and light optical microscope (LOM). Magnetic properties have been investigated by Mössbauer spectroscopy.

Experimental procedure

Specimen preparation and composition analysis

A vacuum induction melting technique under argon atmosphere was employed to produce the Fe–Mn–Si alloy melting with commercial Fe and Mn and the final composition was prepared after adding with a suitable amount of commercial Si to the matrix. The alloy was forged in bar shape. The tensile specimen was machined from the round bar after homogenizing annealing at 1273 K for 60 min followed by air cooling in room temperature. Alloy composition was determined by a Spectrolab M5 type probe microanalysis system. The V and carbon concentration in this alloy was about 0.120 and 0.002 wt%, respectively. The intrusion of carbon cannot be avoided during the fabrication of Fe–Mn–Si based alloys, especially in melting [1, 10]. The composition of newly designed alloy is in Table 1. The SME was examined by means of tensile and bending tests.

Table 1 Alloy composition (wt%)

Fe	Mn	Si	V	Cr	Cu	P	Al	C	Nb	S	Ni
69.270	27.790	2.270	0.120	0.042	0.012	0.008	0.002	0.002	0.002	0.002	0.001

Applied measuring techniques

Differential scanning calorimetry

In order to determine the forward and reverse transformation temperatures and the transformation enthalpies, disk shaped specimen of 61.2 mg from the alloy was prepared in the received state. The calorimetric experiment was performed by means of a computer-controlled Perkin–Elmer Pyris 6 DSC instrument at a rate of 15 °C/min between 0 °C and 300 °C for heating and cooling. The cooling measurement was acted by using liquid nitrogen.

Mössbauer spectroscopy

Table 2 Thermal treatments for Vickers hardness measurements

A	Cooled in air to room temperature
B	Cooled in air to room temperature and then cooled in liquid nitrogen bath
C	Quenched in ice + water
D	Cooled in ıce + alcohol
E	Cooled in liquid nitrogen bath

A thin foil of *specimen A* defined in Table 2 was used which served as absorber for Mössbauer effect and it was applied to study the magnetism and volume fractions of both the martensite and austenite phases. A conventional multichannel constant acceleration spectrometer with an initial strength 50 mCi ^{57}Co radioactive source (diffused in Rh) was used during the investigation at room temperature. A Normos-90 computer program was used to find out the Mössbauer parameters and relative volume fractions of the austenite and martensite phases. The Mössbauer spectra of examined alloys were calibrated with respect to α-Fe foil and isomer shifts were given relative to the center of the α-Fe foil.

TEM

TEM was used to characterize the microstructure, determine the crystal structures, and lattice parameters of constituent phases. The TEM thin foils were prepared by mechanical thinning until 80 μm thickness followed by electropolishing in a Struers Tenupol 3 jet polisher at room temperature with an electrolyte of 20% sulphuric acid and 80% methanol solution under a voltage of 8 V with 0.2 A current, then observed on a JEOL JEM-100CX-II TEM with a double tilt specimen holder operating at 100 kV.

SEM and LOM

The microstructure was observed using SEM and LOM. Electron microscopy was carried out on a Philips XL30 SFEG model SEM equipped with an Oxford Instruments EDS system so the composition analyses of the constituent phases of the microstructures were determined using electron dispersive spectrometry (EDS) in SEM. SEM and LOM specimens were prepared from pieces of the specimens prepared by mechanical polishing of the surface of the specimen followed by an etching with the composition of solution containing 3% Nital to reveal ε martensites and the phases to be clearly distinguished. For the metallographic investigations after annealing for 60 min at 1273 K, specimens labeled as A, B, C and E of thermal treatments given in Table 2 were used. An Olympus GX 51 optical metallograph was used to study the microstructure of specimens.

Tensile test

Tensile testing was conducted in an Instron 5569 test machine by using (29.0 mm × 10.1 mm × 2.5 mm) specimen. The strain was measured by an extensometer. The strain was fixed at 2% for two cycles. The prestrain gauge length, L_{n-1}, the length after tension, L_n, and the length after recovery at a high temperature, L_{n+1}, were measured by a tool microscope. Let n be the number of cycles. The recovery rate, η, representing the shape memory effect, is obtained through the following equation [11]:

$$\eta = (L_n - L_{n+1})/(L_n - L_{n-1}) \tag{1}$$

Each training cycle of the specimen, after being annealed at 900 °C for 360 s and then air cooled, includes 2% tensile strain at room temperature followed by heating to 600 °C, holding for 300 s, and then cooling to room temperature.

During every thermomechanical cycle, Vickers hardness number (VHN) was measured from the average of five VHN. For every cycle, the average VHN before tension, VHN_{n-1}, after tension, VHN_n, after recovery with heating to 600 °C, holding for 300 s and then cooling to room temperature, VHN_{n+1}, were measured by Instron Wolpert Testor 2100.

Bending test

Another way to evaluate the shape memory property is bending test of rectangular specimens of 34.6 × 2.4 × 0.3 mm. Figure 1 shows a schematic diagram of the bending test. Bending tests were used as an effective and relatively simple way of characterizing shape memory behavior [12].

The specimen was deformed at room temperature by bending over a rod shaped metal. The amount of shape recovery was determined for specimen B. For every deformation cycle, the specimen was heated at 600 °C, holding for 300 s after each deformation for an austenitizing treatment over the rod shaped metal. The degree of shape recovery ratio named as also recovery strain was determined by the equation below [12, 13];

$$\eta_{\mathrm{SME}} = (90 - \alpha)/90 \times 100\% \tag{2}$$

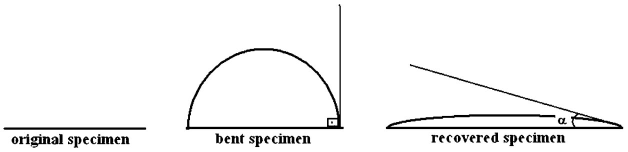

Fig. 1 Illustration of bending test to calculate degree of shape recovery [13]

Vickers hardness measurement

For the hardness measurements independent from the tensile tests, after annealing for 60 min at 1273 K, five different kinds of thermal treatments given in Table 2 were induced to the specimens to see if the material has indeed reached a stable phase structure. The indentation was made on well-polished surfaces of the disk-shaped specimens with a diamond square based pyramid under a load of 10 kgf. In similar with the hardness tests during tensile tests, the measurements were repeated five times to obtain one data point.

Experimental results and discussion

Profile of DSC peaks

The DSC curves for the heating and cooling treatments in the received state for specimen A are given in Fig. 2. The peaks seem to be nearly smooth. This is because training generates dislocation arrays and residual stress in the parent phase in such a way that preferential martensite variants would be nucleated and grown with preferential direction during cooling treatment before DSC investigation. As a result, nearly no bumps can be observed at both endothermic and exothermic peaks [14]. From this curve, M_s, the martensite start temperature, $M_{\max}$, the maximum phase transformation rate temperature, and M_f, the martensite

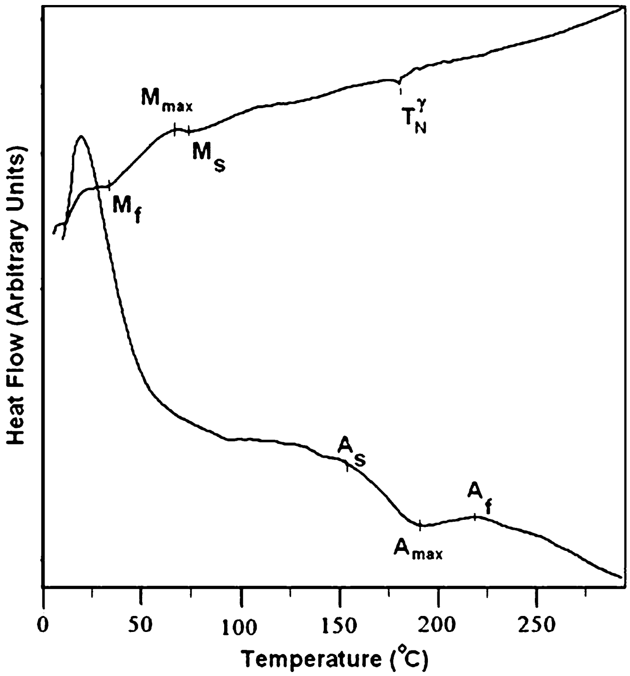

Fig. 2 DSC curve of the specimen showing transformation temperatures

finish temperature were determined as, 74.6 °C, 59.4 °C, and 38.1 °C, respectively and A_s, the austenite start temperature, A_{max}, the maximum phase transformation rate temperature, and A_f, the austenite finish temperature were determined as, 147.4 °C, 183.8 °C, and 220.6 °C, respectively. From the transformation temperatures we can easily see that the difference of $A_{max} - M_{max}$ values is 144.4 °C. Such a big hysteresis is one of the typical characteristics of non-thermoelastic martensitic transformations. The gap between A_s and A_f ($A_f - A_s$) is wider than the gap between M_s and M_f ($M_f - M_s$), which suggests that the driving force needed for the transformation is bigger for austenitic phase.

The fcc(γ) → hcp(ε) transformation in Fe–Mn–Si based alloys may be classified as a semi-thermoelastic martensitic transformation because of the fact that the interface γ–ε, or the Shockley partial dislocation (a/6) <111> can move reversibly but with a thermal hysteresis as high as 100 K. Even if the γ–ε martensitic transformation is non-thermoelastic, Yang et al. [15] noticed a superelastic effect in this type of alloys. Its amplitude depends on the austenitic state and the deformation temperature [16].

Neel temperature, T_N^γ, is 180.7 °C for this alloy as seen in Fig. 2. Neel temperature of this alloy is bigger than M_s temperature. The stabilization of austenite, is caused by the magnetic transformation in the austenitic phase, from paramagnetic at high temperatures to antiferromagnetic below the Neel temperature T_N^γ. The Neel temperature is quite low for low Mn content but increases with increasing Mn content with the result that the curves for T_N^γ, and M_s intersect at a critical Mn content. T_N^γ is above M_s at higher Mn content. At sufficiently large Mn contents, M_s is smaller than T_N^γ, which implies that the fcc phase orders antiferromagnetically before transforming to the hcp phase [17]. Sato et al. found that a complete shape memory effect appears when T_N^γ is lower than M_s. On the other hand, when T_N^γ is higher than M_s, the degree of supercooling increases and the shape memory effect decreases drastically [18]. It can be clearly seen that the specimen which is investigated have a high Mn concentration and so the Neel temperature is higher than the M_s temperature thereby this causes the γ phase to be stabilized by the antiferromagnetic ordering [19, 20]. Shape memory alloys in the Fe–Mn system require a relatively high M_s, to produce a significant amount of ε-martensite at room temperature and a relatively low T_N^γ to prevent the suppression of the martensitic transformation on cooling to temperatures below the ambient points [20].

Also from the heating and cooling curves, the absorbed energy obtained during heating is −0.51 J/g and released energy obtained during cooling is 0.72 J/g. It can be easily seen that the released energy during cooling is nearly equal to the energy absorbed while heating. On the other hand, the relationship between transformation energy and thermodynamic equilibrium temperature can be written as

$$T_0 = \frac{M_s + A_s}{2} = \frac{\Delta H}{\Delta S} \tag{3}$$

where ΔS is the entropy change defined and T_0 is the temperature at which the Gibbs free energy of austenite equals that of martensite [14, 17, 21]. Equation 3 has often been applied to non-thermoelastic martensitic transformations, whereas the thermoelastic case, e.g., in Cu-based alloys, T_0 has been estimated ($M_s + A_f$)/2 [17]. Since the $\gamma \rightarrow \varepsilon$ martensitic transformation in Fe–Mn–X is generally considered as non-thermoelastic, Eq. 3 is adopted in this study. The T_0 value was calculated as 111 °C. ΔS^{M-P}, entropy change of martensite phase to austenite phase is bigger than the ΔS^{P-M}, entropy change of austenite phase to martensite value. This suggests that disorder process is much in cooling than heating.

Mössbauer spectroscopy

Mössbauer spectroscopy technique is used to define the magnetic characteristics of the martensite and austenite phases. The Mössbauer spectra was obtained at room temperature on the *specimen A*. The observed spectra is characterized by a central singlet and a resolved broad sextet as shown in Fig. 3. The central singlet spectra consists of a line with a small hump at the center. This small hump is named as quadrupole splitting. The doublet structure corresponds to an antiferromagnetic ordering structure. This result shows that the magnetic ordering temperature of the sample studied is higher than the room temperature and M_s. Such a doublet can be seen in the spectra, and it displays that the paramagnetic → antiferromagnetic transition occurs in specimen. In Fe–Mn alloy systems, the absolute values of the quadrupole splitting increase with increasing silicon concentration but the quadrupole splitting is small because of the small lattice shrinking and magnetostriction in Fe–Mn–Si alloys. The content of silicon atoms into Fe–Mn alloys has a strong effect on the surroundings of the Fe nucleus [22]. In Mössbauer spectroscopy, antiferromagnetic or ferromagnetic character of materials display a typical sextet whereas paramagnetic structure exhibits only a singlet. Furthermore, α' (bct) martensitic phase is ferromagnetic while ε (hcp) and γ (fcc) phases display paramagnetic character in Fe–Mn–Si alloys [23]. Therefore, in Fig. 3, the sextet belongs to ferromagnetic α' martensite phase as the paramagnetic singlet can be ascribed either to ε martensite phase or to γ austenite phase. The Mössbauer parameters such as isomer shift (δ), hyperfine magnetic field (B_{hf}) with the calculated % volume fractions of phases are given in Table 3. It is almost impossible to sort the paramagnetic ε

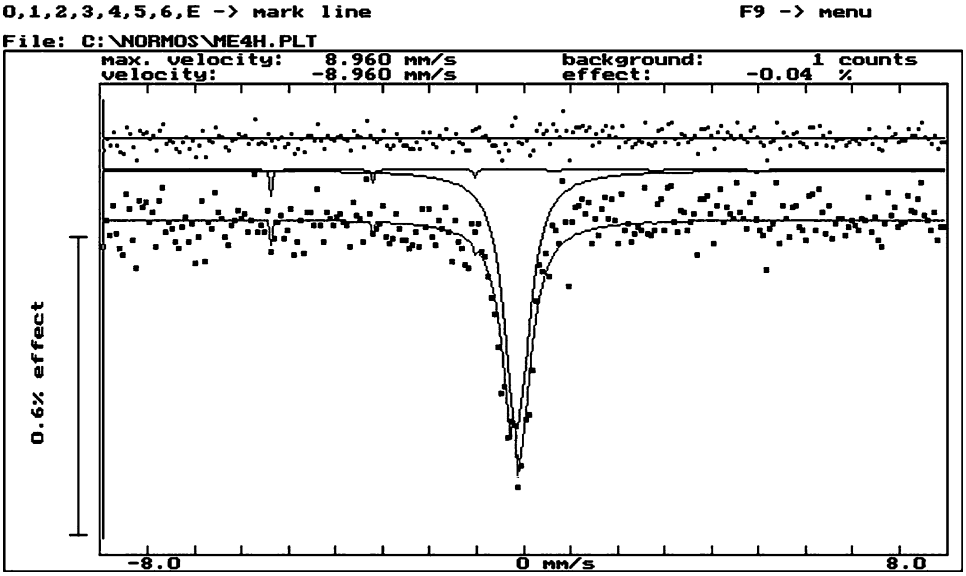

Fig. 3 Mössbauer spectra for the alloy cooled in air

Table 3 Mössbauer parameters of the sample

$\gamma + \varepsilon$ phase (%)	α' phase (%)	$\delta_{\gamma+\varepsilon} \pm 0.002$ (mm/s)	$\delta_{\alpha'} \pm 0.002$ (mm/s)	B_{hf} (α')(T)
98.864	1.136	−0.1392	−0.1964	32.08

and γ phases out by Mössbauer spectrometry at room temperature [23]. Therefore, in Table 3, the volume fractions of ε and γ phases are evaluated together. The amount of α' martensite is very low in the sample as seen in Table 3. As the fraction of α' martensite phase is too small, TEM, SEM, and LOM observations which are discussed below, confirms with Mössbauer results. Therefore, shape memory effect of the alloy may become weak with the formation of α' martensite but the ratio of α' phase in *specimen A* is very low in comparison with γ and ε phases.

TEM observations

TEM study was conducted in order to get a more detailed view of the morphology of crystallites. The result of the TEM morphology observation of the *specimen A* is presented in Fig. 4a, together with its diffraction pattern in Fig. 4b that is taken from the central part of the figure. Thermally induced parallel hcp plates in fcc matrix was observed in specimen. The platelet structure observed within the matrix corresponds to ε martensite. The thin plates appear in one direction as seen in Fig. 4a. Parallel bands on martensite plates that completed their formation can be seen as faint striations. These striations are believed to be caused by stacking faults. This is considered to be due to the nucleation of thin martensite plates that grow successively side by side and coalesce [24].

The martensitic lattice parameters were calculated by means of a simple ratio method from the distances R, between the central spot and the other diffraction spots, camera constant, λL as mentioned below.

$$d = \frac{\lambda L}{R} \tag{4}$$

and the martensitic phase lattice parameters were calculated by means of equation below,

$$\frac{1}{d^2} = \frac{4}{3}\left(\frac{h^2 + k^2 + l^2}{a^2}\right) + \frac{l^2}{c^2} \tag{5}$$

where h, k, and l are the indices; d is the spacing between the individual spaces. The obtained lattice parameters were then slightly improved by comparing them with theoretical and experimental diffraction data obtained from TEM, leading to values of $c_\varepsilon = 4.088$ Å and $a_\varepsilon = 2.541$ Å for ε martensite phase. Accord with this result, the $c_\varepsilon/a_\varepsilon$ value for ε martensite phase is significantly lower than the "ideal" value 1.633 corresponding to a hexagonal close packed arrange of spheres [25].

Microstructural study

Figure 5 shows scanning electron microscope (SEM) images of *sample C*. Figure 5a shows three grains of the austenite and some stacks of small amount of the thermally triggered ε martensite plates placed in the small grain as

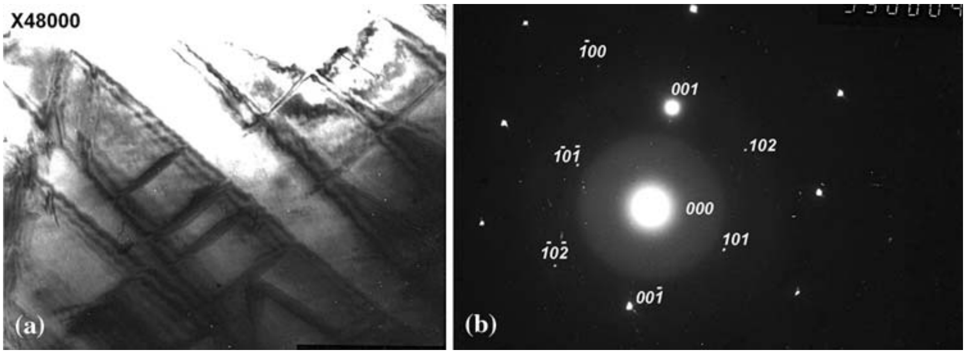

Fig. 4 **a** TEM micrograph showing the formation of thermally-induced ε bands composed by densely parallel stacking faults (48000×) and **b** diffraction pattern of selected area

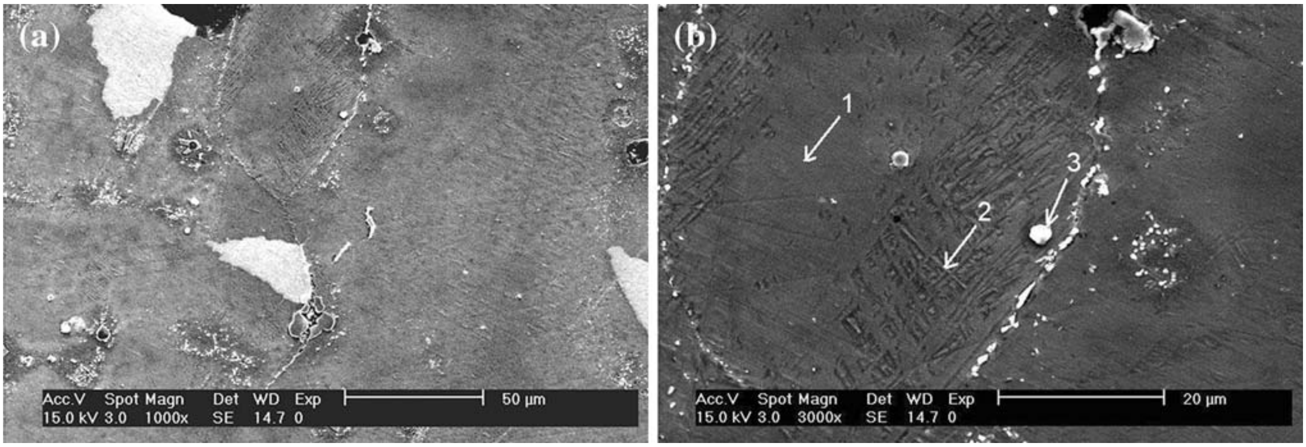

Fig. 5 The SEM image of Fe–27.79Mn–2.72Si (wt%) alloy after water quenching. **a** grain morphology; and **b** austenitic grain matrix, thin ε martensite and discontinuous grain boundary precipitation with pointing out arrow 1, arrow 2, and arrow 3, respectively

seen on the upper part of the micrograph. Figure 5b shows that morphology of ε martensite plates go through austenite grain and also they intersect each other after within the grain and ended at grain boundary. The differences between the austenitic grain matrix, thermally induced martensite and the discontinuous grain boundary precipitation phase are pointed out with arrows as 1, 2, and 3 in Fig. 5b, respectively, and they are obviously determined by using the surface analysis as in Fig. 6.

Specially, the compositions of the small discontinuous buttons placed on grain boundaries must be measured by EDS because they were too small for full chemical analysis. The EDS analysis revealed that the composition of the grain-boundary phase, martensite phase, and matrix had different compositions. According to the EDS analysis result (Fig. 6), it is evident that there is no Carbon in grain matrix shown with arrow 1 (Fig. 5b). As seen in Table 4, the solubility of Carbon in martensite is small but not so small as in austenitic matrix phase. On the other hand, EDS analysis of the grain boundaries (arrow 3) show that the composition was enriched with Carbon while the concentration of Fe falls down.

Concerning the surface topography features, the typical martensite morphology comparison of alloy specimens is presented by the LOM micrograph in Fig. 7. Zhao [13] proved that the SME can be improved significantly by changing the microstructure of the matrix, which can be realized by using a series of heat treatments. The microstructure was found identical. All specimens exhibited a fully recrystallized microstructure resulting from high temperature solution treatment at 1273 K and cooled in different conditions presented in Table 2. All specimens exhibited partial transformation to martensite phase from austenite phase so the heat treated microstructure consists of austenite (γ) grains, ε martensite plates and precipitates occurring at grain boundaries. Optical microscopy also revealed a number of large inclusions in *A*, *B* and *C* specimens after solution treating. The presence of martensite plates in Fig. 7a which means that the specimen is cooled in air, indicates that the start temperature of martensitic transformation M_s is slightly higher than the room temperature. The martensite is observed to form in groups of very thin plates for Fig. 7c and d. Figure 7c illustrates four grains which include a large number of precipitates at

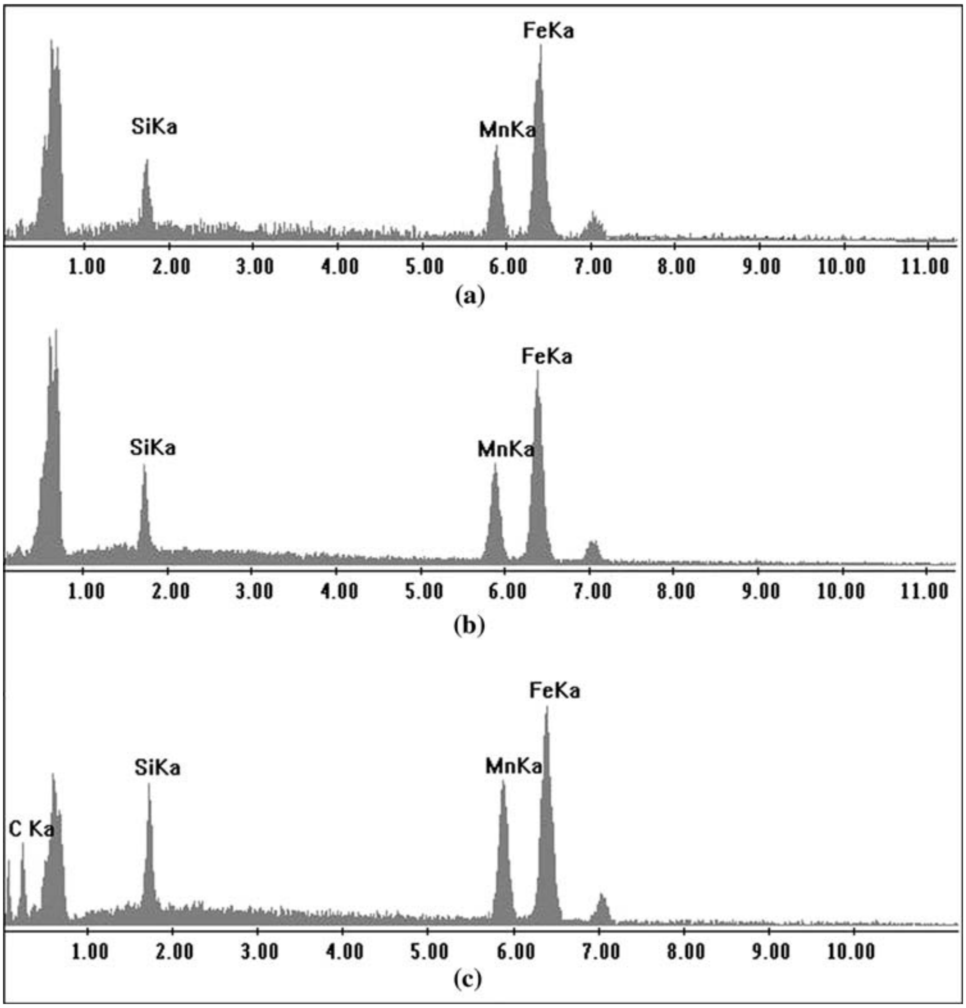

Fig. 6 EDS composition analysis of the re-cast layer: **a** austenitic grain matrix with pointing out arrow 1, **b** thin ε martensite with pointing out arrow 2, and **c** discontinuous grain boundary precipitation with pointing out arrow 3

Table 4 Nominal alloy compositions in weight and atomic percentage measured using EDS

	Fe		Mn		Si		C	
	(wt%)	(at.%)	(wt%)	(at.%)	(wt%)	(at.%)	(wt%)	(at.%)
Austenitic grain matrix	67.16	63.95	28.24	27.33	4.61	8.72	–	–
Thin ε martensite	65.33	59.61	28.57	26.50	4.93	8.94	1.17	4.95
Grain boundary Precipitation	57.49	46.50	32.07	26.37	5.64	9.07	4.80	18.06

grain boundaries. The precipitates were restricted to the grain boundaries, and were elongated along the grain boundaries. The precipitated phase did not form a continuous film, but consisted of discrete particles. Because of the precipitation hardening and the pinning of dislocations caused by the segregation of the alloy atoms, the strength of the matrix increased, which resulted in a very good SME [25, 26]. Figure 7d shows straight lines which are due to the formation of ε lamellar structure martensite plates along $\{111\}_{fcc}$ planes. The surface of the *specimen C* and *E* presents reliefs are composed of many parallel scratches, certainly corresponding to the ε bands which pass through the whole grains from one end of grain boundary to the other. In specimen E, the martensite is formed in groups of very thin parallel sided stacks of plates stopped at grain boundary on the left grain. Many ε martensite plates which intersect each other within the grain with different growing directions were observed in the right side of austenite grain shown in Fig. 7d. From the micrographs, it can be seen that Fe–28.71Mn–2.27Si alloy is composed with γ-austenite and ε-martensite, and interestingly, the volume fraction of ε-martensite is significantly much more than that of γ-austenite in *specimens A*, *B* and *E*. It has been predicted that the number of martensite plates nucleated (formed) in cooled material is directly proportional to the concentration of lattice defects in the austenite phase at the cooling time

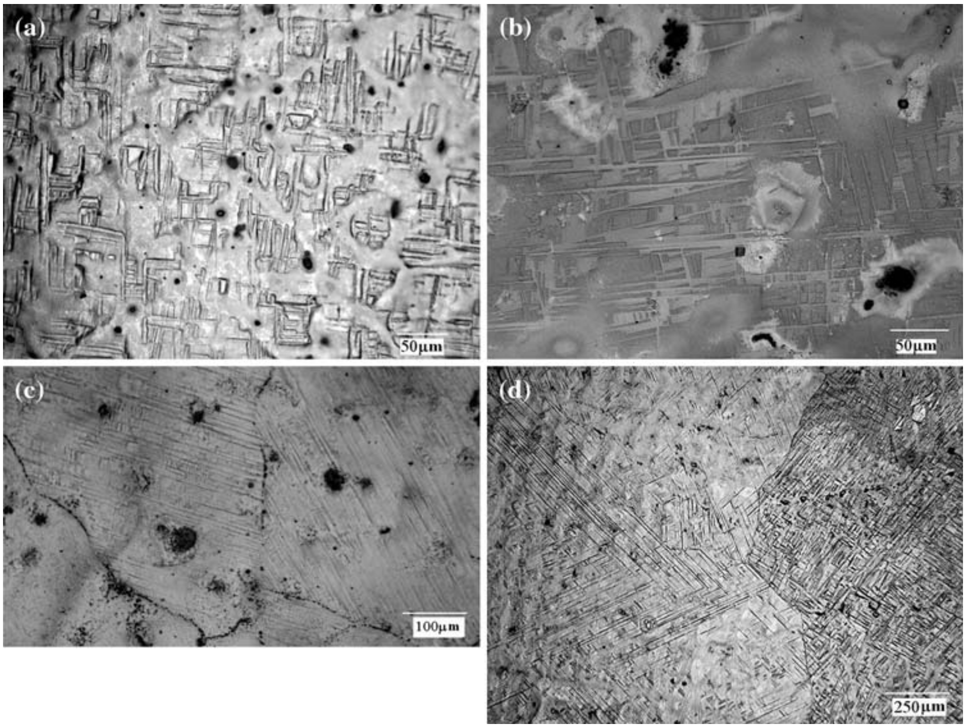

Fig. 7 A series of optical micrographs showing the microstructural changes of the Fe–28.71Mn–2.27Si alloy cooled at various conditions from 1273 K: **a** *Specimen A*, **b** *Specimen B*, **c** *Specimen C*, and **d** *Specimen E*

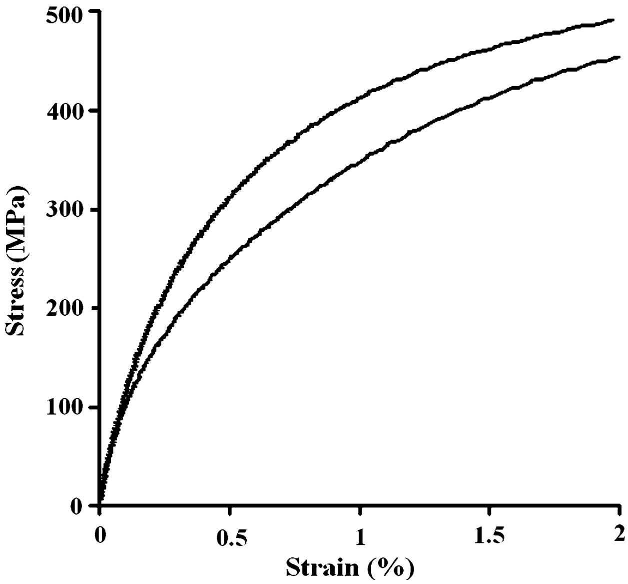

Fig. 8 Stress–strain curves for the strains fixed at 2%

[26]. Figure 7a–d shows that the larger austenite grain size provides the easier formation of ε martensite phase [27].

Relation between thermomechanical cycle and shape recovery rate

Stress–strain curves of the specimen for two cycles of tensile training which include the same strain rate of 2% are shown in Fig. 8. Second cycle has shown a reduction in stress. This stress is required to form martensite for every thermomechanical cycles. The stress reduction may be due to the effect of the elastic stress fields in reducing the nucleation barrier for the second cycle [28]. This decreasing tensile strength is ascribed to the stress relief and grain growth [29].

Table 5 shows the dependence of the shape recovery on thermomechanical cycle for Fe–Mn–Si alloy. It can easily be seen that the shape recovery of the alloy increases with the second cycle. An increase in reversibility with increasing number of thermomechanical cycles is a common feature in most studies. Training or thermomechanical transformation cycling may improve the shape recovery in these alloys but this mechanism is not still clear. Characterization of the transformation behavior during cycling is an important prerequisite for practical use of such alloys [28].

The average hardness numbers of every thermomechanical treatment for the unstrained, tensile strained, and solution-treated sample are also summarized in Table 5. It is so exciting to see that the VHN changes resemble the gauge length changes which were used to calculate the shape memory ratio for every thermomechanical treatment step. The increased hardness is thought to be the effect of the increased dislocation density, and the increasing amount of strain-induced phases [30]. This investigation about hardness may be another way to show the shape memory effect for this type alloys.

Table 5 SME% and average hardness of the specimen for two cycles of strain during the thermomechanical treatments of tensile test

Cycle	Strain (%)	Stress (MPa)	SME (%)	Average Vickers hardness number (VHN)		
				Before strain	After strain	After heating
1	2	490	64	260	295	266
2	2	453	85	266	278	265

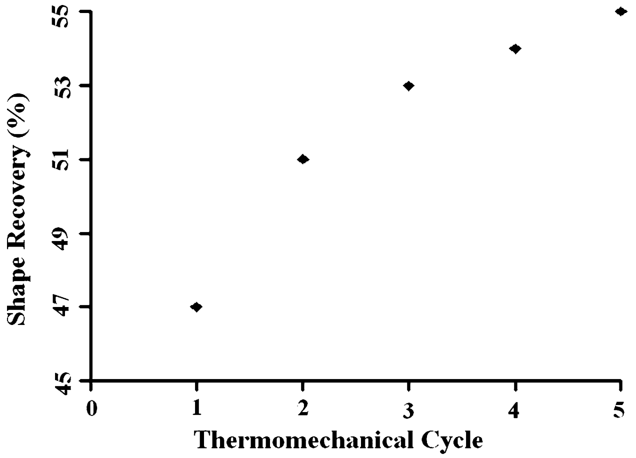

Fig. 9 Effect of thermomechanical treatment (training) for every cycle on SME by bending test

Bending test

The results of the shape recovery of bending tests are summarized in Fig. 9. From the figure, it should be remarked that a 47–55% shape recovery is obtained for five deformation cycles in the case of bending tests. It should be noted that there is an increase in shape memory effect between the first and fifth cycles. Consequently, the shape recovery of the alloy increases after every cycle but one can see clearly that the shape memory effect can be greatly improved after the first training cycle. The training process simultaneously produced dislocations and stacking faults, which increased with an increasing number of training cycles. The stacking faults could act as nucleation sites for the martensite transformation, so the critical stress for the formation of ε martensite decreased. The dislocations impeded the formation and growth of ε martensite, and the heating process eliminated those dislocations [31, 32].

Vickers hardness measurement

The changes in VHN as a function of different thermal treatments are presented in Fig. 10. From the figure, it can be seen that there are two stages. In stage I, the alloy shows low hardness values in thermal treatment A and B; in stage II, there is a high hardness value in thermal treatment C, D, and E, respectively. It can be seen that the specimen's induced different thermal treatments achieve a value of 172 VHN to 237 VHN. It appears that the retained austenite in more slowly cooled samples like thermal treatment A and B is more stable than the C, D, and E specimens.

Putatunta et al. [33] showed that the material after quenching in liquid nitrogen had very high hardness, which is a characteristic of the typical martensitic structure. Increase in hardness in stage II in this work resembles their investigation results. The increase in hardness means the generation of perfect dislocations and was attributed to the introduction of sessile lattice defects that hinder the movement of partial dislocations [34].

Fig. 10 VHN values of different thermal treatments

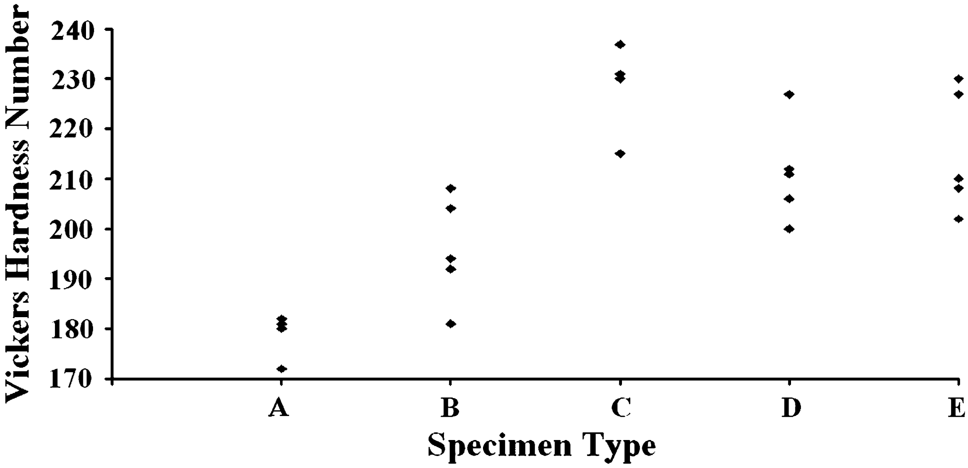

Conclusion

In this article, some calculations of the stresses which are therefore favorable to a good shape memory effect and microstructural images were investigated in Fe–Mn–Si alloy. The following conclusions are considered as being important.

(a) The thermal hysteresis of the transformation temperature is too large. This shows that the transformation is non-thermoelastic but the motion of dislocations act as semi-thermoelastic. Also from the heating and cooling curves, the absorbed energy obtained during heating is nearly equal to the released energy obtained.

(b) Mössbauer spectroscopy result shows that the magnetic ordering temperature of the sample studied is higher than the room temperature and M_s. Also, metallographic investigations showed that the presence of martensite plates in *specimen A* which means that the specimen is cooled in air, indicates that the start temperature of martensitic transformation M_s is slightly higher than the room temperature. DSC results supports all the suggestions above about the martensitic transformation temperatures are close but higher from room temperature.

(c) The calculated volume fractions of α' martensite phase is 1.136% and the total volume fraction of ε and γ phases is 98.864%. The amount of α' martensite is very low in the *specimen A*. As the fraction of α' martensite phase is too small; TEM, SEM, and LOM observations confirms with Mössbauer results. Therefore, shape memory effect of the alloy may become weak with the formation of α' martensite but the ratio of α' phase in the specimen is very low.

(d) The $c_\varepsilon/a_\varepsilon$ value for ε martensite phase is significantly lower than the "ideal" value 1.633 corresponding to a hexagonal close packed arrange of spheres.

(e) The martensite is observed to form in groups of very thin plates for increasing cooling rates. LOM micrographs show that the larger austenite grain size provides the easier formation of ε martensite phase.

(f) *Specimen A* cooled in ice + water include a large number of precipitates at grain boundaries. The precipitates were restricted to the grain boundaries, and were elongated along the grain boundaries. The precipitated phase did not form a continuous film, but consisted of discrete particles.

(g) The shape recovery of the alloy increases with thermomechanical cycles and with every tensile and bending tests.

(h) After a fast cooling process, the material had very high hardness, which is a characteristic of the typical martensitic structure.

Acknowledgements The authors are pleased to acknowledge and thank for the financial support for some investigations of this research by "Firat University Scientific Research Projects Council (FUBAP)", Turkey, under grant no. 775. The authors thank Prof. Dr. Şakir BOR and his assistant Miss Elif TARHAN for their help on TEM investigations.

References

1. Wen YH, Xie WL, Li N, Li D (2007) Mater Sci Eng A 457:334
2. Verbeken K, Van Caenegem N, Verhaege M (2007). doi:10.1016/j.msea.2007.01.188
3. Van Caenegem N, Duprez L, Verbeken K, Segers D, Houbaert Y (2007). doi:10.1016/j.msea.2007.02.159
4. Baruj A, Kikuchi T, Kajiwara S, Shinya N (2004) Mater Sci Eng A 378:333
5. Kajiwara S, Liu D, Kikuchi T, Shinya N (2001) Scr Mater 44:2809
6. Baruj A, Troiani HE (2008) Mater Sci Eng A 481–482:574
7. Baruj A, Kikuchi T, Kajiwara S, Shinya N (2002) Mater Trans JIM 43:585
8. Yang JH, Wayman CM (1992) Acta Metall Mater 40(8):2011
9. Wen YH, Xiong LR, Li N, Zhang W (2008) Mater Sci Eng A 474:60
10. Eskil M, Kanca E (2008) Comput Mater Sci 43(4):774
11. Zhang J, Chen S, Li L, Hsu TY, Xu Zuyao (1998) Mater Charact 40:37
12. Li H, Dunne D, Kennon N (1999) Mater Sci Eng A273–275:517
13. Zhao C (1998) Mater Res Bull 33(10):1433
14. Xu H, Tan S (1995) Scr Metall Mater 33(5):749
15. Yang JH, Chen H, Wayman CM (1992) Metall Trans A 23:1431
16. Bergeon N, Guenin G, Esnouf C (1998) Mater Sci Eng A242:87
17. Cotes S, Sade M, Guillerment AF (1995) Metall Mater Trans A 26A:1957
18. Sato A, Yamaji Y, Mori T (1986) Acta Metall 34(2):287
19. Andersson M, Stalmans R, Agren J (1998) Acta Mater 46:3883
20. King HW, Peters MA (1997) Can Metall Q 36(2):137
21. Tatar C, Yakuphanoglu F (2005) Thermochim Acta 430:129
22. Qin Z, Zhang Y (1998) Hyperfine Interact 116:225
23. Sari U, Kirindi T, Yüksel M, Ağan S (2008) J Alloy Compd. doi:10.1016/j.Jallcom.2008.09.47
24. Marinelli P, Sade M, Guillermet AF (2002) Scr Mater 46:805
25. Maji BC, Krishnan M (2003) Scr Mater 48:71
26. Kayalı N, Özgen S, Adigüzel O (1997) J Phys IV 7(C5):317
27. Kirindi T, Güler E, Dikici M (2007) J Alloy Compd 433(1–2):202
28. Reyhani MM, McCormick PG (1994) Scr Metall Mater 31(7):875
29. Lin HC, Lin CS, Lın KM, Chuang YC (2001) J Alloy Compd 319:283
30. Meszaros I, Prohaszkab J (2005) J Mater Process Technol 161(1–2):162
31. Eskil M, Ceylan M (2005) 4th international advanced technologies symposium, Konya/Turkey, 28–30 Sept 2005
32. Zhao C (1999) Metall Mater Trans A 30A:2599
33. Putatunda SK, Yang J, Gundlach RB (2005) Mater Des 26(6):534
34. Otubo J, Mei PR, Koshimizu S, Shinohora AH, Suzuki CK (1999) Mater Sci Eng A A273–275:533